Nanoscale

Synthesis and Characterization of $MoSe_2$ Nanoscrolls via Pulsed Laser Ablation in Deep Eutectic Solvents

Journal:	*Nanoscale*
Manuscript ID	NR-ART-04-2024-001466.R1
Article Type:	Paper
Date Submitted by the Author:	23-May-2024

Complete List of Authors:	Morales Betancourt, Alejandro; The University of Texas at San Antonio, Physics and Astronomy Flores, Ernesto; The University of Texas at San Antonio, Physics and Astronomy Shaji, S; Universidad Autonoma de Nuevo Leon Nash, Kelly; The University of Texas at San Antonio College of Sciences, Physics and Astronomy

ARTICLE

Synthesis and Characterization of MoSe2 Nanoscrolls via Pulsed Laser Ablation in Deep Eutectic Solvents.

Received 00th January 20xx,
Accepted 00th January 20xx

DOI: 10.1039/x0xx00000x

Alejandro L Morales Betancourt,[a] Sadasivan Shaji,[b] Ernesto Flores,[a] Kelly L. Nash.*[a]

There is ongoing interest in the rapid, reproducible production of 2-dimensional (2-D) transition metal dichalcogenides (TMD), such as molybdenum-based TMD (MoX_2), where X is a chalcogen atom such as sulphur (S), selenium (Se) or tellurium (Te), driven by their unique optical and electronic properties. Once fabricated into an atomically thin layer structure, these materials have a direct-indirect bandgap transition, strong spin–orbit coupling, and favourable electronic and mechanical strain-dependent properties which are attractive for electronics. Pulsed laser ablation in liquid (PLAL) is an economic, green alternative for synthesis of TMD. It has been shown that in the case of MoX_2, the chemical processes during the plasma phase of the ablation can yield the formation of multispecies, including MoO_x quantum dots when oxygen-containing solvents are used. Here, we introduce the formation of $MoSe_2$ nanoscrolls with low oxygen content synthesized via pulsed laser ablation in deep eutectic solvents (PLADES). Our results suggest that the synthesis produces a stable colloidal solution of large 2-D structures with tuneable surface charge by replacing the deep eutectic solvent (DES) with DI water. Nuclear Magnetic Resonance (NMR) results suggest that irradiating the solvent at near infrared NIR energy does not affect its chemical composition. NMR also proves that serial washing can completely remove solvent from the nanostructures. Raman shifts suggest the formation of large, thin $MoSe_2$ nanosheets aided by the solvent confinement resulting from van der Waal forces and hydrogen bonds interactions between $Mose_2$ and urea. Binding energies measured by XPS confirm $MoSe_2$–DES preference to form 1T-$MoSe_2$ versus molybdenum oxides and 2H $MoSe_2$ in DI-water. Raman and XPS findings were validated by transmission electron microscopy (TEM) and selected area electron diffraction (SAED). Results of this work validate the use of PLADES for the synthesis of stable, crystalline, low-surface-oxygen-content colloidal $MoSe_2$ nanoscrolls in scalable quantities.

1. Introduction

The need for automatization of processes and production of microprocessors with novel capabilities has pushed for the search of new materials to be used as semiconductors and develop new techniques for synthesis. In this regard, scalable production of stable colloidal nanostructures that preserve specific characteristics and functionalities is required for the advancement of next-generation electronic devices. Transition metal dichalcogenides TMD have been widely studied and used for semiconductor applications mainly in the form MoS_2. Recently, $MoSe_2$ has been targeted as a great choice of semiconductor due to its short transition from indirect to direct band gap compared to its sulphur-based homolog[1, 2]. Morphology dependency of TMD makes them an interesting class of materials for enhanced applications of optoelectronics and sensing applications, including flexible electronics, energy harvesting devices, biosensors, and catalysts. Some approaches to produce $MoSe_2$ have been based on chemical methods, such as chemical vapor deposition, biological assembly of nanomaterials, and physical methods such as electric deposition and Laser ablation[3, 4]. In particular, mechanical exfoliation of $MoSe_2$ nanosheets from a bulk target has demonstrated to be a rapid reliable way to obtain high yield and consistent nanostructures[5]. Pulsed laser ablation in liquids (PLAL) is a rapid, green, low-cost technique for exfoliation from a bulk material[6, 7]. PLAL uses a light source, focused in a target that breaks to produce nanomaterials taking advantage of the confinement provided by a liquid phase. The parameters to be considered in PLAL include the physical and chemical properties of the target material like state, composition, and grain size; configuration of light source like wavelength excitation, duration of the pulse, and energy fluence; and finally, a liquid phase with specific density, viscosity, and composition[8]. Confinement media plays an important role in the kinetics of nanoparticle (NP) formation, for instance, it is possible to tune the size by changing the properties of the solvent[9]. Despite PLAL's remarkable ability to produce NP, nanosheets (NS), and quantum dots (QD) without ligands, the interaction with the liquid phase can end up with multiple species, especially oxides

[a] Functional Nanomaterials Lab, The University of Texas at San Antonio. Department of Physics and Astronomy, One UTSA Circle, San Antonio, TX, 78249, Email: Kelly.Nash@utsa.edu, Alejandro.moralesbetancourt@utsa.edu, Ernesto.Flores@utsa.edu

[b] Universidad Autónoma de Nuevo León, Faculty of Mechanical and Electrical Engineering, Pedro de Alba SN, Ciudad Universitaria, 66455 San Nicolás de los Garza, N.L., México. Email: Sadasivan.Shaji@uanl.edu.mx

† Footnotes relating to the title and/or authors should appear here.
Electronic Supplementary Information (ESI) available: [details of any supplementary information available should be included here]. See DOI: 10.1039/x0xx00000x

due to the need for stability during aggregation, influencing also the morphologies of NP made of different materials including noble metals and TMD[10-12]. Some reports of $MoSe_2$ synthesized by laser ablation in liquids converge in the formation of spheres with amorphous regions with phases, and defects using isopropanol as liquid phase[13], versus inorganic fullerene-like (IFL) structures obtained in a mixture of 30% ethanol/water[14] Furthermore, a combination of semi-crystalline $MoSe_2$ nanosheets, α-MoO_3, and *h*-MoO_3 QD with amorphous structure have also been identified in water.[15] Also, it has been reported the exfoliation of $MoSe_2$ nanosheets in water using a femtosecond laser pulse.[16] Considering that the functionality of the NP, NS, and QD derives from their morphology, and this depends on the atomic state of the material limiting oxidation during stabilization would provide a new opportunity to increase the capabilities of PLAL. Surface oxidation is a recurrent state that widely influences the electronic properties of nanomaterials. TMD's electronic transitions are contingent to morphology, enhancing the search for new ways to achieve pristine surfaces. The formation of oxides of materials ablated in DI water has been observed, in agreement with the oxidation degree dependency on the material's redox potential[17]. To produce nanoalloys while minimizing the undesired oxides, some organic solvents like acetone and toluene with reducing chemical potentials are preferred[18, 19], however, some of them can form coats of carbon layers on the nanoparticles. In general, using organic compounds as a liquid phase of laser ablation has an impact on the functionalization of the nanomaterials surface[20]. In this study, we showcase the effectiveness of PLAL in producing TMD while mitigating surface oxidation, utilizing a deep eutectic solvent (DES) as a confinement medium. Henceforth, referred to as pulsed laser ablation in deep eutectic solvents (PLADES) within this research. This kind of solvents have diverse physical characteristics that make them a more complex environment to confine the nanostructure formation because it presents lower vapor pressure and lower conductivity compared with water[21].

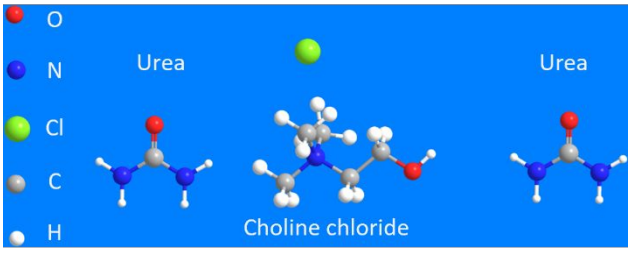

Figure 1. Structure of Reline, consisting in two molecules of Urea per one of choline chloride.

Reline, a liquid solution of choline chloride and urea in a 1:2 molar ratio remains liquid at room temperature due to hydrogen bonding. Physicochemical properties of this type of DES have been modelled and explained in terms of its water content[22]. It has been suggested that the use of DES as a media for NP's growth has a size limiting effect[23]. For instance, using reline as a liquid phase, silver nanoparticles have been produced by laser ablation obtaining smaller sizes than those prepared in water[24]. Furthermore, some metal oxides like CuO, Cu_2O, ZnO, and PbO can dissolve in ChCl:Urea environment that are attributable to complex formations with urea and decomposition products[25]. To the extent of our knowledge, the combination of pulsed laser ablation using a deep eutectic solvent as a liquid phase has not been reported to produce a $MoSe_2$ or any other binary colloidal nanostructures. This combination opens the possibility to rapid mass fabrication of Oxygen-free suspended TMD nanostructures to be used in electronic and catalytic processes, due to the reline lower oxygen content per volume of about 50 percent of that found in water. For systemic simplicity most of the PLAL-related dynamic studies are recorded using water as a liquid phase, however, the inclusion of a solvent with different physicochemical properties helps to reduce the oxygen content and multi-speciation of $MoSe_2$ nanostructures.

2. Experimental

2.1 Materials and methods.

Liquid phase preparation. 40 mmol of reline with a final volume of 8.7 ml was prepared from a 2:1, urea-choline chloride molar ratio following the protocol in Abbott et al. 2003[26]. Reagents were independently dried in a vacuum oven at 110°C overnight to remove water, then mixed on a hotplate at 80°C while stirring at 900 rpm, until a clear homogeneous solution was obtained. **Target and vessel preparation.** 50mg of $MoSe_2$ powder 99.9% trace metals basis with a MW of 253.86 g/mol and a melting point >400°C (Sigma-Aldrich, USA) was placed in a conical glass test tube. 0.5 ml of DES at 60°C was added to the tube to cover the target. The tube was then placed in a vacuum oven at 70°C and 0.1 atm for two hours to remove any air bubbles generated within the target. The tube was capped with a glass coverslip and sealed with parafilm to prevent the interaction with cold air and limit evaporation during ablation. **Laser ablation.** For irradiation, we use a pulsed Nd-YAG laser (EKSPLA NT342B, Lithuania) with a fundamental wavelength of 1064 nm, with pulse duration of 3.6 ns, and a repetition rate of 20Hz at a fluence of ~24 Wcm^{-2}. The laser beam is focused from above at the target with a convex lens with 300mm focal distance. The pulse rate is maintained at 20Hz for 15 minutes. To decrease the refractive index of the DES, a Polystat© (Cole-Palmer) was used to maintain the sample submerged in a 70° C water bath during the ablation. This step also reduces the viscosity of the reline and ensures a better transport of the ablated materials. At this temperature reline pH is ~8, conductivity is ~6 $mScm^{-1}$ and the mixture will absorb water spontaneously due to its hydroscopic nature[27]. Using other solvents, increasing the temperature only affects the size distribution of the produced nanostructures[28]. After the first irradiation (1st Ab), the supernatant was transferred to a secondary tube. The colloidal solution was exposed to a second irradiation using the same laser parameters as the first irradiation, except that the beam was focused at the mid-depth of the solution to produce 2nd nano solution (2nd Ab). We repeat the same process using DI water as a liquid phase, to have a base to compare the nanomaterials produced in Reline. To establish differences between the synthesized materials the terms pulsed laser

ablation in liquids (PLAL) and pulsed laser ablation in deep eutectic solvents (PLADES) will be used to define synthesis in DI water (H_2O) and reline respectively.

2.2 Characterization

Size and Surface charge by Dynamic Laser Scattering (DLS). After first and second ablation, size and zeta potential of the nanoparticles was assessed using a Zetasizer nano-ZS system (Malvern, United Kingdom). Samples were diluted by 20-fold in DI water. The measurements were conducted by triplicate and then averaged and plotted in Origin software. **Nuclear Magnetic Resonance** was performed in the $MoSe_2$–DES produced nanoparticles suspension right after first and second irradiation treatment, and after a series of washing steps of the $MoSe_2$–DES sample. J values are given in Hz.δ_H(500 MHz, D_2O). All samples were diluted in a 4:1 ratio into deuterated water and then analysed in a Bruker 500 MHz Advance III HD spectrometer (Bruker, MA, USA). **Micro Raman** samples for 1st and 2nd Ab of PLAL and PLADES synthesis were prepared in a 5x7 mm silicon wafer placed in a microcentrifuge tube with 1ml of colloidal solution, followed by centrifugation at 24K RFC for 60 minutes. All the samples were measured by triplicate at different locations then averaged. Measurements were carried out using an iHR320 Horiba Jobin Yvon spectrometer (Kyoto, Japan) operated at a laser excitation wavelength of 785 nm, focused using a 10x magnification lens for probing and signal collection. The spectrometer was equipped with a Grating of 1200g/mm, and a Synapse CCD detector. **X-ray Photoelectron Spectroscopy (XPS)** was assessed using a K-Alpha X-ray Photoelectron Spectrometer System (Thermo Scientific, UK) equipped with a monochromatic Al Kα X-ray source with 1486.7 eV energy, with a spot size of 400µm. For close range acquisition, a step size of 0.1eV and a pass energy of 50 eV was used. Spectra was corrected using 284.6 eV as a reference peak of adventitious carbon (Adv.C). To keep the integrity of the materials to be analysed by XPS, molybdenum diselenide 2nd Ab solution in water ($MoSe_2$-W) and molybdenum diselenide 2nd Ab solution in deep eutectic solvent ($MoSe_2$-DES) were mounted in a 5x7 mm silicon also by centrifugation. Data was processed and analysed using Avantage Software (Thermo Scientific). **Transmission electron microscopy (TEM).** Morphology and crystallinity of the nanostructures were assessed by JEOL 2010-F (Akishima, Japan) equipped with a Selected Area Electron Diffractometer (SAED). Micrographs and diffraction patterns were analysed using Gatan Micrograph (Pleasanton, CA) and CrysTBox software[29] (Institute of Physics of the Czech Academy of Sciences, Czechia) respectively.

3. Results and discussion

3.1 Synthesis and Characterization of $MoSe_2$ by PLADES ($MoSe_2$ - DES) and PLAL ($MoSe_2$ -W).

The production of colloidal $MoSe_2$ nanomaterials from bulk was identified after the first pulsed laser irradiation at 1064 nm due to a distinct change in the colour of the liquid phase from clear to brownish, for both samples $MoSe_2$ -W and $MoSe_2$-DES *(Figure 2a)*. In DES the solution seems to be a lighter brown with a visible gradient of increasing concentration from the bulk to the liquid-air interphase. This layer remains until the end of the first irradiation *(Figure 2a top-left).* This interlayer gives a clue about the nature of the effective confinement of the plasma plume and therefore the synthesis mechanism that yields ionization of the target over photo fragmentation as described by many authors while investigating the effects of laser in the target[30, 31]. Explosive boiling of the target can also be deduced because there is an accumulation of ablated material in region near the light quid-bulk interphase as it is expected after 15 minutes of irradiation. Furthermore, the viscosity of the solvent helps to visualize the convection process occurring to form the gradient temperature between the superheated ablated material and solvent from the cooler region away from the focal point, this pattern agrees with what has been described by the transport of the ablated material in the synthesis vessel[32]. After the secondary beam laser irradiation in DES, the solution becomes a homogeneous darker brown colour (fig 1.a top-right). The reason for the colour change is the effect of laser fragmentation in liquids (LFL) that aids in narrowing the size distribution as measured by dynamic light scattering (DLS), compared to the first irradiation *(Figure S1).* In contrast, $MoSe_2$ –W, the sample ablated in DI water shows a homogeneous red-brown colour *(Figure 2.a bottom-left)*. Attenuation of the beam due to accumulation of colloidal nanoparticles in the solution is common even in short laser exposures[33, 34] during PLAL. Such effect affects the kinetics of nanoparticle formation by broadening the size distribution due to the change in light fluence on the target[7]. After secondary irradiation, the solution becomes lighter, and orange red *(figure 2.a bottom-right)*, suggesting a process of laser fragmentation in liquids (LFL) of the colloidal nanostructures. LFL was confirmed by ***Dynamic Light Scattering (DLS)***. In the case of the DES, there is a bimodal size distribution of the $MoSe_2$ nanostructures after the first irradiation with peak at 550 nm, and the distribution turns to single mode after second exposure reducing the average size to 450 nm. For the first irradiation in DI water, normal size distribution was recorded with peak at 150 nm, however after the secondary irradiation, the peak shifted to 120 nm, but the distribution becomes bimodal *(Figure S-1)*. Since reline is less polar than water[35], and considering that less polar liquids yield larger sized nanoparticles[36], the $MoSe_2$ nanosheets form bigger in DES than in water; furthermore, the morphology was largely affected showing structure of nanosheets in the case of DES and spherical nanoparticles in DI water *(Figure 2.b)*. This could be an effect of the weak van der Waals forces aided by the hydrogen bonding nature of DES acting as a template to convey large nucleation sites. However, in DI water this process seems to be stalled due to hydration that limits the growth during ripening due to the early stabilization of the nanoparticle's surface (probably) by oxide layers. Formation of oxides in the surface of the nanoparticles yields large ***Zeta potential (ZP) values.*** $MoSe_2$-DES surface charge was negative but with a very small value of -1.5 and -0.3mV for 1st and 2nd respectively. Both first and second irradiation of $MoSe_2$-DES samples also present a secondary peak at positive values of 35.06 and 39.88mV

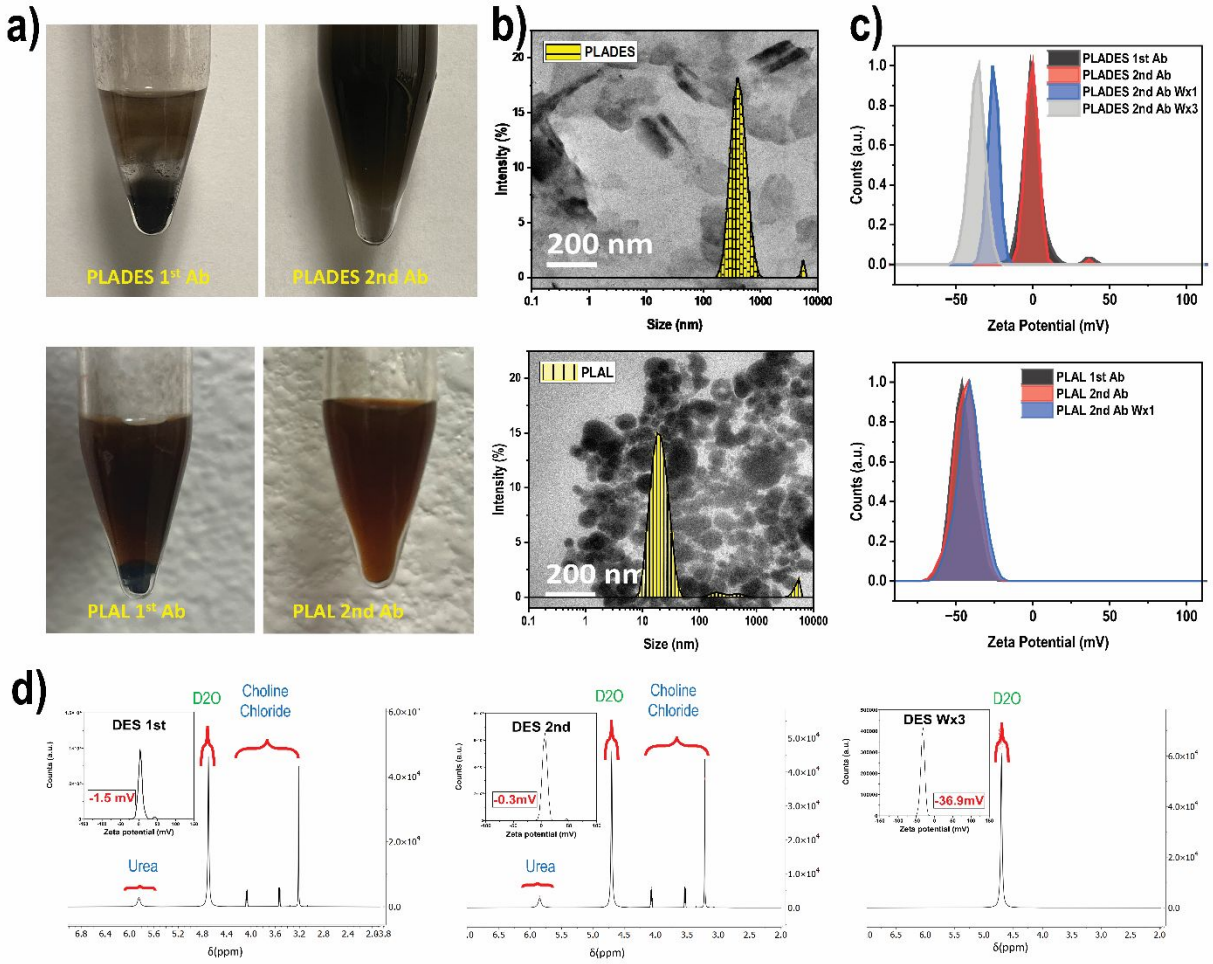

Figure 2. **a)** Images of the $MoSe_2$-DES and $MoSe_2$-W nano colloid solutions after first and second irradiation of $MoSe_2$ powder in reline (top) and water (bottom) **b)** Transmission electron micrographs) of the nanoscrolls obtained in DES (top) and spherical nanoparticles by PLA in water (bottom) (size distribution corresponds to the dynamic size measured by dynamic light scattering. **c)** Stability of the colloidal structures measured by zeta potential (ZP) surface. **d**). HNMR confirms the successful removal of urea and choline chloride from the $MoSe_2$-DES sample.

respectively. Small ZP is commonly referred as charge neutralization, and it is attained when the solution pH reaches the isoelectric point[37]. Bimodal ZP distribution has been explained by electro-kinetic retardation and enhancement, also present in samples with multimodal size distribution at pH 10[38]. This coupled effect may occur by the interaction of the nanoscrolls with the solvent, which surrounds the particles but are larger than common solvent ions. This effect has been studied in the macroscale where deep eutectic solvent shows strong electrostatic attraction between its cations and the negative charged material, suggesting a compression of the electrical double layer, resulting in a lower zeta potential measurement[39]. Surface charge measured after three successive washing steps becomes more negative showing values of -26.3 and -36.9 mV for first and third washing steps, respectively *(figure 2.c top)*. $MoSe_2$-W colloids display a negative zeta potential charge with a sharp peak at -46.2 and -42.2mV for first and second laser irradiation respectively *(figure 2.c bottom)*. These high negative zeta potential values have been assigned to the presence of metal oxides (MoO_x), and are present in both 1st and 2nd irradiation. These results suggest a tendency towards the formation of nanostructures with reduced oxygen content when using deep eutectic solvent even as earlier as after first irradiation. **Nuclear Magnetic Resonance (NMR)** was used to further investigate the effect of the DES on the surface charge fluctuations towards larger negative ZP values after washing steps (figure 2.d). Since the NMR signature of the Reline components differs from the signature attributable to other complexes containing Se or Mo, assessing purification of the $MoSe_2$-DES is straightforward. No chemical shift change was detected during washing steps δ_1 5.98(s,D_2O, 4H), 4.13(m, J = 2.8 Hz, 2H), 3.62(t, J = 5.0 Hz, 2H), 3.31(s,D_2O, 9H,). Furthermore, the relative abundance also remains the same between purification until third wash, when the presence of reline is no longer evident and the ZP value becomes more negative. To understand if laser irradiation has an impact on the chemical shift of deep eutectic solvent, neat reline was irradiated under the same conditions used during ablation, but without the MoSe2 target. No change in resonance frequency of the Reline was identified, after irradiation, suggesting that exposure of the DES to NIR wavelength does not induce molecular decomposition or solvent degradation *(Figure S-2)*.

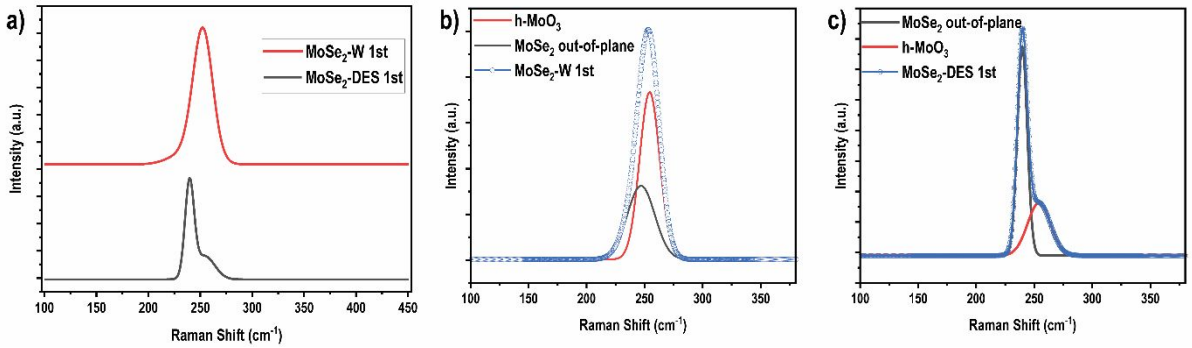

Figure 3. Raman spectra of MoSe2 in water and deep eutectic solvent after first irradiation(a). Deconvolution of sample synthesised in water with of overlapping Raman bands corresponding to vibrational modes of MoSe2 and h-MoO3 (b). Deconvolution of sample synthesised in deep eutectic solvent with sharp band in the out of plane vibrational mode of MoSe2 and broad band shoulder corresponding to h-MoO3 (c).

Furthermore, no shifts in the spectra of pure solvent and nano colloidal solution were detected confirming that energy input only interacts with the $MoSe_2$ and that there is no adsorption of the solvent on the nanostructures surface (*Table S-1*). Thus, leaving an intact, stable solvent after irradiation, even in the presence of a bulk material. **Micro Raman Spectroscopy**. In order to have a better understanding of the material transition during 1st ablation we measured the Raman shift of the colloidal ablated material after 1st irradiation of both samples (Figure 3.a). Deconvolution of spectra of sample ablated in water ($MoSe_2$-W 1st), shows a sharp peak at 254cm^{-1}, overlapping with a peak at 246 cm^{-1}. The first corresponds to vibrational mode of h-MoO_3, and the second to the A_{1g} out-of-plane vibrational mode of $MoSe_2$ (Figure 3.b). In the case of deep eutectic solvent ($MoSe_2$-DES 1st), there is a narrow band with large intensity at 239 cm^{-1}, along with a low intensity broad band with peak centred at 254 cm^{-1}, at the location of vibrational modes of out-of-plane $MoSe_2$ and MoO_x species, respectively (Figure 3.c). There is no visible band corresponding to the E_{2g} in-plane vibrational mode, suggesting the formation of thin-layered structures in both syntheses[40]. The results suggest an early tendency for oxides formation in $MoSe_2$-W 1st sample, compared to $MoSe_2$-DES 1st. The spectra of the second irradiation over the region of interest of $MoSe_2$ is shown in figure 4.a. Active vibrational modes are expected in the region near to 240 cm^{-1} and 280 cm^{-1} for out-of-plane and in-plane respectively. Deconvolution of broader peaks in the position of characteristic $MoSe_2$ out-of-plane A_{g1} vibrational modes shows low intensity peak at a Raman shift at 239.14 cm^{-1} for $MoSe_2$-W and a high intensity peak at 239.93 cm^{-1} for $MoSe_2$–DES (Figure 4.b). Raman shift peaks with comparable intensities of E_{g2} in-plane vibrational mode appear at 280.85cm^{-1} and 281.63 cm^{-1} for $MoSe_2$–W and $MoSe_2$–DES respectively. Wagging vibrational modes of α-MoO_3 are present in $MoSe_2$–DES sample, as it is denoted by a peak at 290.47cm^{-1}, with intensity similar to that of the E_{g2} $MoSe_2$ in-plane mode[41] *(Figure 4.c)*.The presence of h-

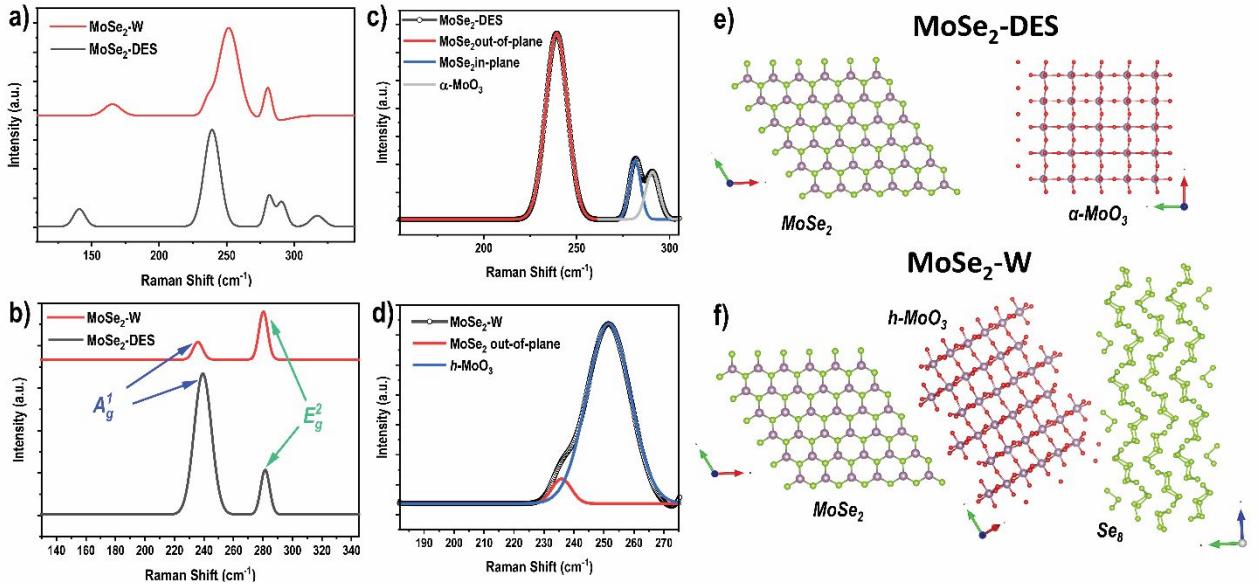

Figure 4. Raman spectra of $MoSe_2$ in water and deep eutectic solvent after second irradiation (a). Characteristic peaks corresponding to the in-plane and out-of-plane vibrational mode of $MoSe_2$ (b). Deconvolution of the E^2_g region of $Mose_2$ of $MoSe_2$-DES sample suggest the presence of α-MoO_3 (c). Deconvolution of the A_{g1} of $MoSe_2$-W sample shows a broad peak within the known Raman shift of *h*-MoO_3 and Se_8 vibrational modes(d).). Graphic representation of the species revealed by micro-Raman analysis of the nanostructures produced by $MoSe_2$-W (e) and $MoSe_2$-DES (f).

MoO_3 species is suggested by the high intensity peak at 253.36 cm^{-1} for $MoSe_2$–W *(Figure 4.d)*. In the case of $MoSe_2$–W sample at larger shifts, a peak at 336.15 cm^{-1} corresponds to A_g bending modes of layered α-MoO_3[42]. A redshift in the $MoSe_2$ A_{1g} vibrational mode has been associated with a decrease in number of layers. The relative intensity of the in-plane and out-of-plane bands are related to the thickness of layered $MoSe_2$. A larger A^1_g/E^2_g intensity ratio denotes the presence of thinner layers in the DES case. In the case of synthesis in water, the presence of high intensity peak at the h-MoO_3 region imply an abundance of oxidation of Mo, although other species may coexist. According to the Raman theory, bands representing stronger bonds will vibrate at larger frequencies, as well as lighter atoms, then the broad band at ~250 cm^{-1} from the water sample can also be interpreted as overlapping molybdenum oxide and long chains of polymeric Se_μ[43]. The vibrational modes of both $MoSe_2$ and α-monoclinic selenium Se_8 are too close to the h-MoO_3 counterpart and made difficult to resolve the Raman spectra, and further analysis is needed. Figures 4.e and f show a representation of the structures expected to be produced by PLADES and PLAL according to the Raman results.

X-Ray photoelectron spectroscopy energy peaks of the closed range regions were assigned based on the position and main geometric differences between spin-orbit splitting in the C1s peak *(figure 5.a and d)*. Results of Mo3d for $MoSe_2$–DES and $MoSe_2$ –W samples are displayed into the energy window 224-240 eV. For $MoSe_2$–DES, the peaks at 227.93 eV for the $Mo3d_{5/2}$ and its $Mo3d_{3/2}$ component at 230.98 eV, for a spin-orbit splitting of 3.05 eV were assigned to the formation of 1T $MoSe_2$ nanosheets, as previously described in literature at binding energies (BE) of ~228 eV[44], compared with the higher BE of 2-H $MoSe_2$ *(figure 5.b and e)*. A secondary doublet with similar splitting energy peaks at 231.39 and 234.44 eV. This secondary set with broader distribution corresponds to small quantities h-MoO_3, and other MoO_x bonding[45], both cases in agreement to micro Raman results. A third doublet with different symmetry at 227.04 eV was assigned to metallic Mo. This peak shows narrow distribution due to its strong bonding nature, compared to those assigned to $MoSe_2$, in which case the reason for a broadening is the coordination, resulting in an electronic screening typical of semiconductors. A single peak corresponding to Se3s was also recorded in the same range at 229.4 eV. On the other hand, $MoSe_2$ –W sample shows a high intensity doublet at 231.63 eV and 234.80 eV, corresponding to the Mo^{6+} $3d_{5/2}$ and $Mo3d_{3/2}$ respectively with a spin orbit splitting of 3.17 eV suggesting large amounts of Mo-O bonding[46, 47]. Secondary set of peaks of the deconvoluted fit, expressed a doublet with its 5/2 orbit component centred at 228.9 eV and 3/2 at 231.95 eV that has been assigned to the Mo^{4+} 3d state corresponding to $MoSe_2$, although this value also overlaps to the binding energy of other Mo oxidation states[48], and the broad peak includes the region for $MoSe_2$. Selenium binding energies for the Se3d region were recorded between 51-62 eV *(figure 5.c and f)*. $MoSe_2$–DES shows a doublet with peaks at 53.95 and 54.77 eV that correspond to the spin orbit splitting of $Se3d_{5/2}$ and $Se3d_{3/2}$[49]. There is a secondary doublet needed to fit the shoulder region with 5/2 component at 54.18 eV. The presence of secondary peaks suggests the formation of

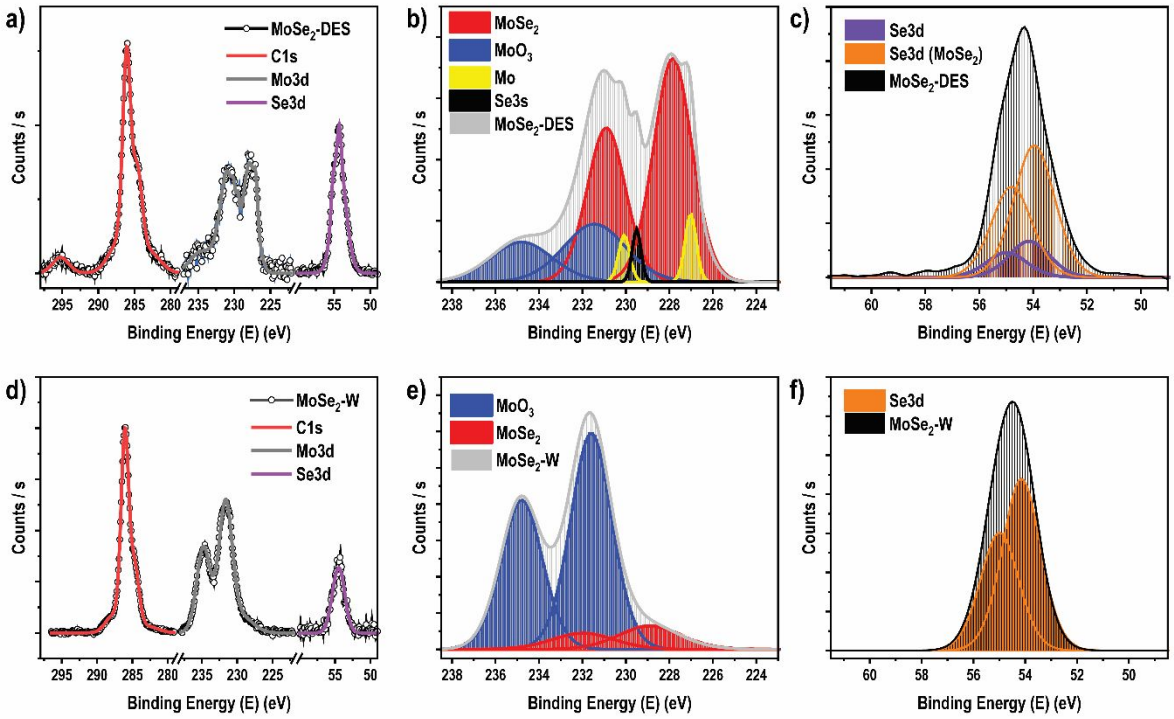

Figure 5. XPS spectra of $MoSe_2$ samples prepared by pulsed laser ablation in deep eutectic solvent ($MoSe_2$-DES) and DI water ($MoSe_2$-W) for the closed regions C1s, Mo3d and Se3d synthesis (a and d). Deconvolution of the Mo3d region in $MoSe_2$-DES (b) and $MoSe_2$-W (e). Closed regions scan of Se3d for $MoSe_2$-DES and $MoSe_2$-W samples (c and f).

other $MoSe_x$ species. Unlike the PLADES synthesized sample, $MoSe_2$-W $Se3d_{5/2}$ shows a peak at 54.13 eV with its orbital splitting at 54.97 eV, corresponding to its $Se3d_{3/2}$ doublet. Spin orbit splitting of Se3d for both samples were 0.84+/-0.02 eV in agreement with that largely reported to be ~0.86 eV[49-52]. According to the Mo:Se ratio we determine the stoichiometric for the $MoSe_2$–DES surface samples is closer to that of $MoSe_2$ than the $MoSe_2$–W synthesized sample. It is also remarkable the large shift in binding energies between samples, discarding similar species. After edging there is a small shift towards 227.68 and 228.78 eV and their corresponding doublets were assigned to the $Mo3d_{5/2}$ of $MoSe_2$ and MoO_2 for the $MoSe_2$–DES sample, while on the $MoSe_2$ –W two sets of peaks with $Mo3d_{5/2}$ spin orbits at 227.01 and 228.72 eV were assigned to Mo metal and $MoSe_2$, respectively. In addition, a peak corresponding to Se 3s was identified at 226.66 eV revealing nevertheless, the formation of $MoSe_2$*(figure S-3)*. These results give further explanation to the Raman results, where Mo oxides were identified, and seem to confirm the hypothesis of formation of nanostructures in a Se depleted region in $MoSe_2$ –W in comparison to PLADES. Such localized depletion favours the formation of MoO_3 and polymeric Se_μ. Fitting the corrected charge using carbon was a challenge for two main reasons, the presence of carbon species intermixed with the $MoSe_2$–DES sample and the possibility to find a C-Se assigned at 284.9 eV that has been described to occur in the presence of porous carbon-$MoSe_2$ heterostructures[53]. In the case of $MoSe_2$–DES, it is assumed that small quantities of organic compound remain interlinked between $MoSe_2$ nanosheets. Also, in this energy window, Se Auger peaks have been reported to occur at 287 and 299 eV leading to an error of the C1s reference for charge correction[50]. Some authors have assigned the position of metallic Mo3d at ~ 228 eV with spin orbit splitting that have a ratio other than the 2/3 for compounds formed by Mo. Nevertheless, $MoSe_2$ has also been assigned to binding energies smaller than 228.0 eV, with a 2/3 ratio. In the presence of other MoO_x species (common Mo oxide is Mo_4O_{11}) the broadness of the peak may differ due to peak overlap and poor resolution to deconvolute the peaks[51]. **Transmission Electron Microscopy (TEM).** $MoSe_2$–DES sample shows larger structures in the form of nanosheets in agreement to the DLS results. These structures are crystalline and have still present some spherical particles assigned to oxides *(Figure 6.a).* The large sheet shown in figure 6.b presents a very ordered crystal lattice with Se-Se interplanar distance of 3.3 Å corresponding to the 1T $MoSe_2$(figure S-4 and S-5). Diffraction pattern analysis shows planes $\bar{2}\,1\,1$ and $1\,1\,\bar{5}$, corresponding to the $MoSe_2$ crystal lattice at the [2 3 1] zone axis (*Figure 6.c*). The TEM micrographs of $MoSe_2$-DES validate the Raman and XPS results where $MoSe_2$ nanosheets were suggested along with small amounts of oxides. In contrast, spherical nanoparticles present in the $MoSe_2$-W TEM micrographs have been identified in the literature as MoO_x and small $MoSe_2$ nanosheets[54] *(Figure 7.a)*. Those structures present a broad size range validating the measured size distribution by Dynamic Light Scattering and reinforce the zeta potential measurements attained by surface stabilization by rapid oxidation. The overwhelming number of spheres also corresponds to the MoO_3 species and the presence of small nanosheets that validate the vibrational modes of $Mose_2$ measured by micro-Raman and the binding energies assigned to Mo3d region in the XPS analysis *(Figure 7.a)*. The semi-crystallinity recorded by DP validates the formation of multiple species in $MoSe_2$–W samples identifying reflections corresponding to planes (0 2 0), (2 1 0) of MoO_3 along with planes (0 0 3), (0 1 4) and (0 1 7) of $MoSe_2$ lattices *(Figure 7.c)*. Also, in the $MoSe_2$ –W large crystal structures in the form of nanoneedles were found *(Figure 7.d)*. According to the Raman results, the composition of these needles belongs to long chains of Se_8 and Se_μ forming Se nanoneedles (SeNN) *(Figure 7.e)*. This validates the Raman analysis of overlapping peaks in the region where Se_8 and MoO_3 converge. Se depletion due to jet ejections in the vicinity of plasma plume and the cavitation bubble, may be responsible for the formation of oxides by $MoSe_2$ –W in high vapour pressure H_2O[42]. The ejected selenium then reaches a secondary zone for nanoparticle formation away from the nucleation sites of Mo causing the formation of selenium needles. The separation of the two materials in different density gradients may result by the difference in thermal stability and

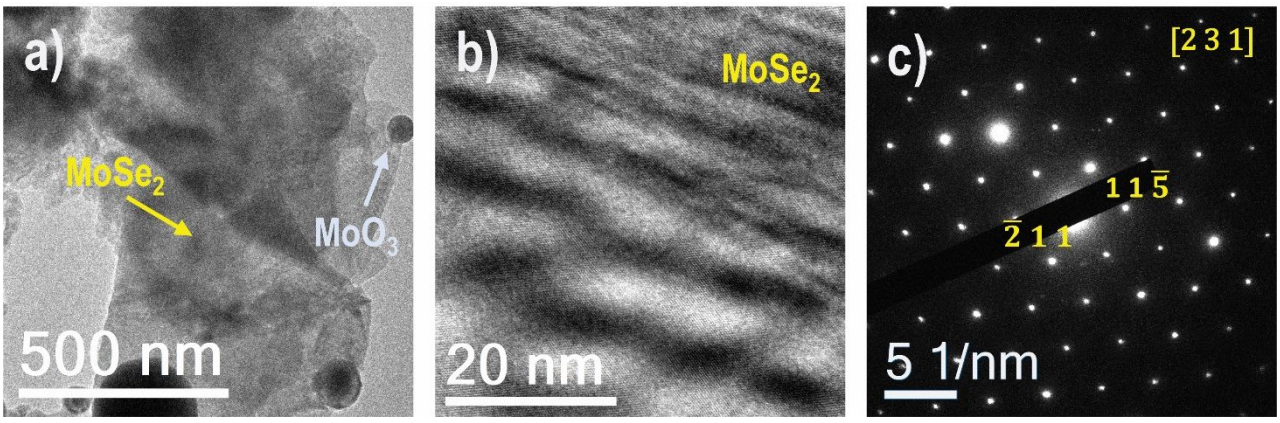

Figure 6. TEM micrographs and diffraction pattern of the $MoSe_2$-DES synthesized nanostructures. Large Nanosheets of $MoSe_2$ in the presence of some spherical nanoparticles suggest a preference for the formation of two-dimensional structures in deep eutectic solvent (a). Wavy planes within the nanosheets show strain along the sheets due to van der Waals forces between misaligned layers of $MoSe_2$ (b). Diffraction pattern of Large nanosheets confirms the formation of large crystalline $MoSe_2$ structures (c).

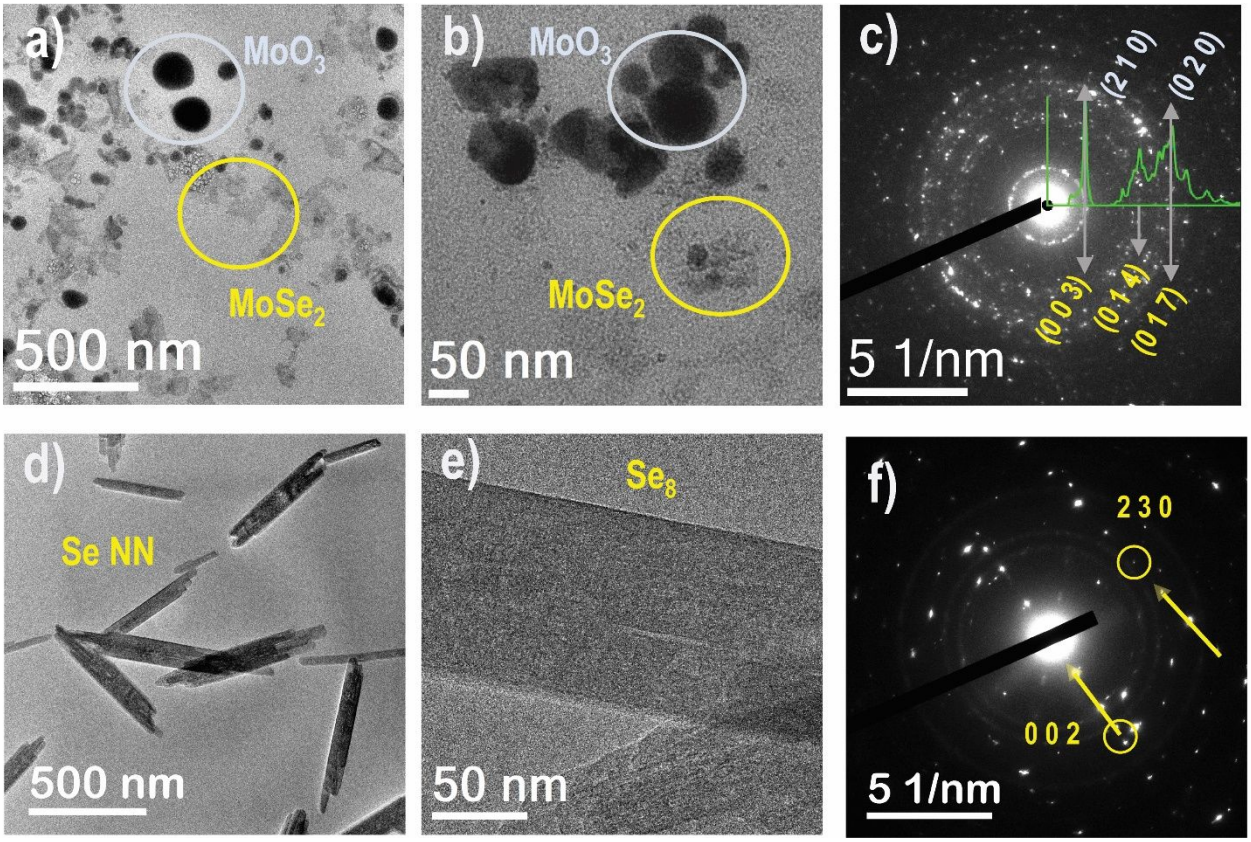

Figure 7. TEM analysis of the MoSe2-W synthesized nanostructures. A combination of spherical nanoparticles and small nanosheets in the synthesis with DI water, suggests the formation of multiple species by the interaction with the free oxygen of the system and the hydration of the nanomaterials (a-b). Analysis of diffraction pattern (DP) of the entire region shows a combination of polycrystalline structures of h-MoO3 (grey) and MoSe2 (yellow) (c). Isolated selenium (Se) nanoneedles have been identified also during the PLAL synthesis, suggesting the growth of Se in regions apart from MoO_x nucleation sites (d-e). Selenium structure was confirmed to be Se_8 by DP (f).

transition temperature which for selenium is at a lower order of magnitude. The presence of Se needles has been recently reported to be fabricated by laser ablation of elemental Se in organic solvents like ethanol, acetone, and toluene[55]. There is no report of these structures in water, at low pulse frequencies. Instead, high pulse frequencies in the order of kHz were used, suggesting a direct relationship between frequency and aspect ratio. In agreement with those results, SeNN of about 500nm length were observed in this work, an expected aspect ratio by the lower frequency used for ablation (20Hz). DP analysis shows reflection of the {0 0 2} and {2 3 0} family planes corresponding to Se_8 in a region close to the [3 2 0] zone axis *(Figure 7.f)*. The presence of such structures suggests an alternative for the kinetics occurring during early stages of the PLA in DI water, where large quantities of selenium are segregated from the nucleation sites of molybdenum that forms oxide complexes aided by the abundance of free oxygen gas released from water during ablation process.

3.2 Discussion

The product of $MoSe_2$ powder pulsed laser ablation in deep eutectic solvents (PLADES) has shown a unique morphology. Micrographs of $MoSe_2$ -DES reveal the development of scroll-like formations with a more confined size range, consistent with DLS findings, indicating the emergence of monocrystalline 2D TMD nanostructures, with at least one of their dimensions is less than 200nm, suitable for semiconductor applications. This is characteristic of nanosheets, which grow along the plane of the sheet, leading to the bending of the edges and resulting in scroll-like structures reminiscent of rolled paper [56]. In this study, the process behind the formation of $MoSe_2$ nanoscrolls is thought to be influenced by the interlayer van der Waals forces acting perpendicularly to the surface of the sheets. This process is aided by the hydrogen bonding forces of the deep eutectic solvent keeping individual to low thickness nanosheets, as suggested by Raman results. The accumulation of interlayer forces overcomes the dynamic hydrogen bond interactions of the solvent, causing deformations at the edges of long sheets. Such deformations increase as the layers roll on themselves. The solvent also plays an important role by yielding preferential growth of nanosheets and excluding formation of oxide structures, due to the low oxygen content as XPS results confirm. In the conventional approach, Pulsed Laser Ablation in Liquids (PLAL) is typically performed at ambient temperature, given the rapid timescale at which binary nanoparticle systems reach thermodynamic equilibrium [57-59]. Within this context, the introduction of moderate (~70C) heating of the liquid phase during PLADES is unlikely to significantly affect the mechanistic stages of the ablation process (e.g. plasma plume formation, fragmentation, ejection, etc.) or yield temperature driven phase transitions of produced materials. This observation is infrequently discussed in the broader literature, with a few

exceptions noted[60]. Nevertheless, the impact of elevated temperature on solvent behaviour, which subsequently influences oxide formation, should not be overlooked [61]. Specifically, in Deep Eutectic Solvents (DES), temperature increments can modulate the pH of the solvent. A reduction in oxidized species may be linked to the pH of the liquid phase; for instance, Fe oxides do not form at pH values above 8, yet their formation is favoured in the pH range of 5-8 [62]. This suggests that the cause of oxide formation could be attributed to the pH in the conventional synthesis temperature range. In the PLADES synthesis setup, the pH of reline drops from approximately 10 to 8 as the temperature rises from ambient to 70°C. This change is due to the increased kinetic energy of the solvent, leading to more frequent ionic collisions and resulting in H+ dissociation [27]. This proton dissociation may also be the cause of attenuation of H-bonding in the solvent allowing van der Waals forces to lead the scroll formation. In the case of the synthesis with water, spherical nanoparticles commonly form as a mixture of $MoSe_2$ and MoO_x species, exhibiting a wide size distribution, with most particles being smaller than 100 nm. This indicates the creation of various zero-dimensional (0D) and one-dimensional (1D) species. $MoSe_2$ nanospheres result from the more stable configuration during the initial growth and aggregation at short time scale of pulse irradiation. This morphology has been observed not only in Mo oxides produced through pulsed laser ablation in liquids but also in other synthesis methods, including hot wire vapor deposition and electrochemical reduction[63-65]. The difference in morphology and chemical composition found during Raman, XPS and TEM characterization suggest that there is a relevant change for the production of TMDC specifically MoSe2 by pulsed laser ablation in deep eutectic solvents compared with the widely used DI water. This study will open the opportunity to increase the benefits of pulsed laser ablation in this type of solvent for the production of more uniform layered materials with low oxygen content in the search for new applications in different fields like colloidal semiconductors, flexible electronics and biomedical.

4. Conclusions

In summary, employing deep eutectic solvents (DES) as the liquid medium for MoSe2 synthesis via pulsed laser ablation has facilitated the assembly of thinner layers. The hydrogen bonding characteristic of DES plays a crucial role in promoting the formation of larger, more crystalline structures compared to those synthesized in water-based solvents. This synthesis approach showcases distinctive scroll-like formations indicative of monocrystalline 2D Transition Metal Dichalcogenide (TMD) nanostructures, with dimensions suitable for semiconductor applications. The process is influenced by interlayer van der Waals forces and hydrogen bonding of the solvent, leading to the bending and rolling of nanosheets resembling paper scrolls. pH modulation due to temperature increment impacts oxide formation, emphasizing the role of pH in conventional synthesis. In contrast, water synthesis yields MoSe2 nanospheres alongside MoO_x species. Given the diverse size and morphology requirements of nanoparticles (NPs) for various applications, it underscores the necessity for developing new synthesis methods that cater to the evolving demands for semiconductors with novel physical properties.

Conclusively, the $MoSe_2$-DES synthesis method has demonstrated its effectiveness in producing novel scroll-like $MoSe_2$ nanosheets (NS). The method not only successfully identified the charge hindrance in $MoSe_2$ NS but also provided a comprehensive understanding of this phenomenon through detailed purification steps, including serial washing. The analysis of colloidal solutions using Hydrogen Nuclear Magnetic Resonance (HNMR) was instrumental in confirming the elimination of DES, and to discard solvent degradation during laser irradiation. The structural integrity of $MoSe_2$ NS was extensively verified using a variety of techniques, such as Raman spectroscopy, XPS, TEM, and diffraction patterns. The utilization of DES as the liquid phase in pulsed laser ablation showcased a notable decrease in the formation of undesired species, such as MoO_x and polymeric Se8, compared to ablation in deionized water emphasizes the advantages of PLADES. Moreover, through zeta potential and NMR analysis, it was demonstrated that serial washing effectively removes DES, yielding 2-dimensional $MoSe_2$ that can be readily resuspended in solvents for potential applications. This purification process ensures the maintenance of a stable colloidal suspension of nanosheets produced in DES, further showcasing the method's efficacy. Additionally, the versatility of the PLADES approach is highlighted, presenting a suitable method for synthesizing powders without necessitating further purification or the production of bulk material pellets. This comprehensive study affirms the PLADES synthesis method's efficiency and advantages in nanomaterial fabrication.

5. Author Contributions

Alejandro Morales Betancourt, Writing – Original Draft, conceptualization, data curation formal analysis investigation, methodology, data collection. Ernesto Flores, Data collection. Dr. Kelly Nash, project administration, conceptualization, Resources, Funding Acquisition, Writing – Review & Editing. Dr. Sadasivan Shaji, Resources, Data Curation, Writing – Review & Editing.

Supplemental Information

Supplemental Information available on website.

Conflicts of interest

There are no conflicts to declare.

Acknowledgments

This material is based upon work supported by the National Science Foundation Graduate Research Fellowship Program under Grant No.1645627. This work has been partially funded by Clarkson Aerospace Corp. (AFOSR Subaward) under Grant

Number FA9550-21-1-0460. Thank you to the Kleberg Advanced Microscopy Center for their assistance in the capture of micrographs and Raman spectroscopy. Thank you to Dr. Teja Guda and the Biomedical Engineering Department at UTSA for allowing the use of their facilities/software to analyse XPS data.

Notes and references

1. A. Goldberg, A. Beal, F. Levy and E. Davis, *Philosophical Magazine*, 1975, **32**, 367-378.
2. J. Kang, S. Tongay, J. Zhou, J. Li and J. Wu, *Applied Physics Letters*, 2013, **102**, 012111.
3. X. Wang, Y. Gong, G. Shi, W. L. Chow, K. Keyshar, G. Ye, R. Vajtai, J. Lou, Z. Liu and E. Ringe, *ACS nano*, 2014, **8**, 5125-5131.
4. J. C. Shaw, H. Zhou, Y. Chen, N. O. Weiss, Y. Liu, Y. Huang and X. Duan, *Nano Research*, 2014, **7**, 511-517.
5. A. Mallouky and J. Bernede, *Thin Solid Films*, 1988, **158**, 285-298.
6. A. V. Kabashin and M. Meunier, *Journal of Applied Physics*, 2003, **94**, 7941-7943.
7. A. Hahn, S. Barcikowski and B. N. Chichkov, *Pulse*, 2008, **40**, 50.
8. S. Barcikowski, V. Amendola, M. Lau, G. Marzun, C. Rehbock, S. Reichenberger, D. Zhang and B. Gökce, *Handbook of Laser Synthesis & Processing of Colloids*, Universität Duisburg-Essen Duisburg, Germany, 2019.
9. H. J. Jung and M. Y. Choi, *The Journal of Physical Chemistry C*, 2014, **118**, 14647-14654.
10. M. Kanazawa, P. Koinkar, K.-i. Murai, T. Moriga and A. Furube, 2019.
11. V. Amendola and M. Meneghetti, *Physical chemistry chemical physics*, 2009, **11**, 3805-3821.
12. T. Oztas, H. S. Sen, E. Durgun and B. l. Ortaç, *The Journal of Physical Chemistry C*, 2014, **118**, 30120-30126.
13. F. Ye, A. Ayub, R. Karimi, S. Wettig, J. Sanderson and K. P. Musselman, *Advanced Materials*, 2023, 2301129.
14. X. Wu, X. Tian, T. Chen, A. Zeng and G. Yang, *Nanotechnology*, 2018, **29**, 295604.
15. A. Balati, A. Bazilio, A. Shahriar, K. Nash and H. J. Shipley, *Materials Science in Semiconductor Processing*, 2019, **99**, 68-77.
16. S.-J. An, Y. H. Kim, C. Lee, D. Y. Park and M. S. Jeong, *Scientific reports*, 2018, **8**, 12957.
17. S. Reichenberger, G. Marzun, M. Muhler and S. Barcikowski, *ChemCatChem*, 2019, **11**, 4489-4518.
18. G. Cristoforetti, E. Pitzalis, R. Spiniello, R. Ishak, F. Giammanco, M. Muniz-Miranda and S. Caporali, *Applied surface science*, 2012, **258**, 3289-3297.
19. L. M. Frias Batista, E. Kaplan, C. Weththasingha, B. Cook, S. Harris, A. Nag and K. M. Tibbetts, *The Journal of Physical Chemistry B*, 2023, **127**, 6551-6561.
20. M.-R. Kalus, R. Lanyumba, N. Lorenzo-Parodi, M. A. Jochmann, K. Kerpen, U. Hagemann, T. C. Schmidt, S. Barcikowski and B. Gökce, *Physical Chemistry Chemical Physics*, 2019, **21**, 24239-24239.
21. A. P. Abbott, D. Boothby, G. Capper, D. L. Davies and R. K. Rasheed, *Journal of the American Chemical Society*, 2004, **126**, 9142-9147.
22. E. O. Fetisov, D. B. Harwood, I.-F. W. Kuo, S. E. Warrag, M. C. Kroon, C. J. Peters and J. I. Siepmann, *The Journal of Physical Chemistry B*, 2018, **122**, 1245-1254.
23. V. Raghuwanshi, M. Ochmann, F. Polzer, A. Hoell and K. Rademann, *Chemical Communications*, 2014, **50**, 8693-8696.
24. D. O. Oseguera-Galindo, R. Machorro-Mejia, N. Bogdanchikova and J. D. Mota-Morales, *Colloid and Interface Science Communications*, 2016, **12**, 1-4.
25. Y. T. Tan, G. C. Ngoh and A. S. M. Chua, *Bioresource technology*, 2019, **281**, 359-366.
26. A. P. Abbott, G. Capper, D. L. Davies, R. K. Rasheed and V. Tambyrajah, *Chemical Communications*, 2003, 70-71.
27. F. S. Mjalli and H. Mousa, *Chinese journal of chemical engineering*, 2017, **25**, 1877-1883.
28. J. Johny, S. S. Guzman, B. Krishnan, J. A. A. Martinez, D. A. Avellaneda and S. Shaji, *Applied Surface Science*, 2019, **470**, 276-288.
29. M. Klinger and A. Jäger, *Journal of applied crystallography*, 2015, **48**, 2012-2018.
30. S. Reich, A. Letzel, A. Menzel, N. Kretzschmar, B. Gökce, S. Barcikowski and A. Plech, *Nanoscale*, 2019, **11**, 6962-6969.
31. V. Amendola and M. Meneghetti, *Physical Chemistry Chemical Physics*, 2013, **15**, 3027-3046.
32. M. Dell'Aglio, R. Gaudiuso, O. De Pascale and A. De Giacomo, *Applied Surface Science*, 2015, **348**, 4-9.

33. A. Bogaerts and Z. Chen, *Spectrochimica Acta Part B: Atomic Spectroscopy*, 2005, **60**, 1280-1307.
34. J. König, S. Nolte and A. Tünnermann, *Optics Express*, 2005, **13**, 10597-10607.
35. A. Pandey, R. Rai, M. Pal and S. Pandey, *Physical Chemistry Chemical Physics*, 2014, **16**, 1559-1568.
36. B. Goekce, D. D. van't Zand, A. Menéndez-Manjón and S. Barcikowski, *Chemical physics letters*, 2015, **626**, 96-101.
37. S. Karmakar, *Recent Trends Mater. Phys. Chem*, 2019, 117-159.
38. Z. Xu, J. Liu, J. Choung and Z. Zhou, *International Journal of Mineral Processing*, 2003, **68**, 183-196.
39. H. Jia, P. Huang, Q. Wang, Y. Han, S. Wang, F. Zhang, W. Pan and K. Lv, *Fuel*, 2019, **244**, 403-411.
40. P. Tonndorf, R. Schmidt, P. Böttger, X. Zhang, J. Börner, A. Liebig, M. Albrecht, C. Kloc, O. Gordan and D. R. Zahn, *Optics express*, 2013, **21**, 4908-4916.
41. N. Hiraoka and Y. Cai, *Synchrotron Radiation News*, 2010, **23**, 26-31.
42. L. Seguin, M. Figlarz, R. Cavagnat and J.-C. Lassègues, *Spectrochimica Acta Part A: Molecular and Biomolecular Spectroscopy*, 1995, **51**, 1323-1344.
43. S. Yannopoulos and K. Andrikopoulos, *The Journal of chemical physics*, 2004, **121**, 4747-4758.
44. R. Zhou, H. Wang, J. Chang, C. Yu, H. Dai, Q. Chen, J. Zhou, H. Yu, G. Sun and W. Huang, *ACS Applied Materials & Interfaces*, 2021, **13**, 17459-17466.
45. B. Brox and I. Olefjord, *Surface and interface analysis*, 1988, **13**, 3-6.
46. S. Jana, S. Ray and S. Mukherjee, *ACS Applied Nano Materials*, 2021, **4**, 1877-1885.
47. T.-J. Dai, X.-D. Fan, Y.-X. Ren, S. Hou, Y.-Y. Zhang, L.-X. Qian, Y.-R. Li and X.-Z. Liu, *Journal of materials science*, 2018, **53**, 8436-8444.
48. D. Xiao, D.-L. Bao, X. Liang, Y. Wang, J. Shen, C. Cheng and P. K. Chu, *Applied Catalysis B: Environmental*, 2021, **288**, 119983.
49. Y.-R. Lin, W.-H. Cheng, M. H. Richter, J. S. DuChene, E. A. Peterson, C. M. Went, Z. Y. Al Balushi, D. Jariwala, J. B. Neaton and L.-C. Chen, *The Journal of Physical Chemistry C*, 2020, **124**, 22893-22902.
50. C. P. Cullen, O. Hartwig, C. Ó. Coileáin, J. B. McManus, L. Peters, C. Ilhan, G. S. Duesberg and N. McEvoy, *arXiv preprint arXiv:2106.07366*, 2021.
51. V. Singh, D. J. Late, A. Goyal and S. Rath, *Applied Surface Science*, 2021, **538**, 147946.
52. S. Xiong, S. Wang, Z. Li, Z. Zhang, H. Liu, J. Wang, L. Hou, Y. Wang and F. Gao, *Chemical Engineering Journal*, 2023, **475**, 146187.
53. N. Li, M. Liu, Y. Ma, Q. Chang, H. Wang, Y. Li, H. Zhang, B. Liu, C. Xue and S. Hu, *ACS Applied Materials & Interfaces*, 2021, **13**, 54274-54283.
54. N. Zamora-Romero, M. A. Camacho-Lopez, M. Camacho-Lopez, A. R. Vilchis-Nestor, V. H. Castrejon-Sanchez, S. Camacho-Lopez and G. Aguilar, *Journal of Alloys and Compounds*, 2019, **788**, 666-671.
55. A. Rahman, B. Krause, T. B. Hoang and G. Guisbiers, *ACS Applied Nano Materials*, 2023, **6**, 2258-2265.
56. M. Kaneda, W. Zhang, Z. Liu, Y. Gao, M. Maruyama, Y. Nakanishi, H. Nakajo, S. Aoki, K. Honda and T. Ogawa, *ACS nano*, 2024.
57. C.-Y. Shih, M. V. Shugaev, C. Wu and L. V. Zhigilei, *Physical Chemistry Chemical Physics*, 2020, **22**, 7077-7099.
58. A. Tymoczko, M. Kamp, C. Rehbock, L. Kienle, E. Cattaruzza, S. Barcikowski and V. Amendola, *Nanoscale Horizons*, 2019, **4**, 1326-1332.
59. M. Kamp, A. Tymoczko, U. Schürmann, J. Jakobi, C. Rehbock, K. Rätzke, S. Barcikowski and L. Kienle, *Crystal Growth & Design*, 2018, **18**, 5434-5440.
60. F. Waag, B. Gökce and S. Barcikowski, *Applied Surface Science*, 2019, **466**, 647-656.
61. V. Amendola, D. Amans, Y. Ishikawa, N. Koshizaki, S. Scirè, G. Compagnini, S. Reichenberger and S. Barcikowski, *Chemistry–A European Journal*, 2020, **26**, 9206-9242.
62. B. Morgan and O. Lahav, *Chemosphere*, 2007, **68**, 2080-2084.
63. S.-H. Lee, R. Deshpande, D. Benhammou, P. A. Parilla, A. H. Mahan and A. C. Dillon, *Thin Solid Films*, 2009, **517**, 3591-3595.
64. N. Dighore, S. Jadhav, P. Anandgaonker, S. Gaikwad and A. Rajbhoj, *Journal of Cluster Science*, 2017, **28**, 109-118.
65. N. Zamora-Romero, M. A. Camacho-Lopez, A. R. Vilchis-Nestor, V. H. Castrejon-Sanchez, G. Aguilar, S. Camacho-Lopez and M. Camacho-

Lopez, *Materials Chemistry and Physics*, 2020, **240**, 122163.